Control of Chloride Ion Corrosion by MgAlO x /MgAlFeO x in the Process of Chloride Deicing

Dongdong Wang
Heilongjiang University
Qi Zhu (hdzhuqi@126.com)
Heilongjiang University
Zipeng Xing
Heilongjiang Univercity
Lei Fang
Haerbin University: Harbin University

Research Article

Keywords: MgAlOx/MgAlFeOx, anti-corrosion, corrosion inhibitor, adsorption, freezing point

Posted Date: June 7th, 2021

DOI: https://doi.org/10.21203/rs.3.rs-467285/v1

Abstract

The corrosion inhibitor that is added to chloride deicing salt, whose anti-corrosion and low pollution is great significance. LDHs, calcined at high temperature were used as adsorbents to remove various anionic contaminants and it could reduce the solution's freezing point after adsorbing anions. Therefore, this paper reports the use of calcined LDHs as corrosion inhibitors in deicing salts. We analyzed that the removal ability of chloride ion $MgAlFeO_x$ was stronger than that of $MgAlO_x$, reaching 85.50%, and the freezing point was lower than that of $MgAlO_x$, the value was -12.0 °C. At the same time, we also found that $CaCl_2$-$MgAlO_x$ and $CaCl_2$-$MgAlFeO_x$ significantly reduce the corrosion of carbon steel and concrete compared with chloride salts, and $CaCl_2$-$MgAlFeO_x$ has the lowest corrosion degree. Hence, we determined that $MgAlFeO_x$ was corrosion inhibitor in chloride deicing salt. The metal molar ratio, synthesis temperature and calcination temperature for preparation of MgAl/MgAlFe-LDHs were determined by XRD and TG-DSC analysis that are 9/2/1, 120 ºC and 500 ºC, respectively. The characteristics of $MgAlFeO_x$ after Fe^{3+} addition were studied in detail by Zeta, XRD, XPS, BET and SEM. The mechanism of corrosion inhibitor's anticorrosion was determined, which was achieved by adsorption and neutralization.

1. Introduction

In order to prevent or mitigate the traffic influence and hazards caused by snowfall in winter, it is necessary to quickly remove snow and ice from the road surface. At present, the methods of deicing mainly include human and mechanical deicing, thermal deicing, chemical melting ice, and active snow prevention technology, etc. Because chemical deicing is the fastest way to remove ice and snow, so, it is the most widely used. Chemical deicing is achieved by using deicing salts (Hao et al. 2019). Because the mixed deicing salt has a low freezing point and little impact on the environment, therefore, it has been interested by the deicing departments of various countries (Nixon 2015; Warner and Ayotte 2015). However, with the extensive use of deicing salts, it is highly corrosive to concrete and steel in infrastructure,such as roads, airports and bridges (El-Nahhal and Lagaly 2003; Farnam 2015). The cause of corrosion is attributed to chloride ions. Due to the small ionic radius, chloride ions penetrates into the concrete with the solution, thus achieving the purpose of breaking the internal structure of the concrete and corroding the metal surface. This is a long-term cumulative process (Farnam et al. 2015a). It is necessary to reduce the corrosion of the infrastructure on the basis of ensuring rapid deicing of the mixed deicing salt. Therefore, many researchers have done a lot of research on the corrosion inhibitors in deicing salt, and it is concluded that the addition of corrosion inhibitors greatly reduces the erosion of Cl^- (Farnam et al. 2015b; El-Nahhal et al. 2005).

In general, corrosion inhibitors are classified into three categories according to their chemical composition. inorganic corrosion inhibitor mainly composed of chromate, nitrite, silicate, etc., whose main function is to passivate the surface of the metal. Although it has remarkable anti-corrosion effect, but its biodegradability is low. Therefore it can cause secondary environmental problems (Ruza et al.

2019). The organic corrosion inhibitors' way of anti-corrosion is to prevent corrosive substances from approaching the surface of the infrastructure through physical adsorption and chemisorption. They are some heterocyclic compounds such as polyvinyl amide, phosphonic acid and polyaspartic acid (Tiu and Advincula 2015), and the anti-corrosion effect is achieved by the combination of polar groups and non-polar groups with the metal of the surface of the infrastructure in the form of certain bond (Amin et al.2010). Organic compounds have well corrosion inhibition effects and are environmentally friendly. However, it will combine with the surface of the object to appear "salt dirty" and affect the aesthetics of areas such as roads (Silva et al. 2006). In addition, there is polymer corrosion inhibitor, such as polyethylene, POCA, etc., which have good corrosion inhibition and can be biodegraded, but they also can adsorb on the surface of the object (Benchikh et al. 2009). In summary, the current corrosion inhibitor added to the deicing salt has the problem is secondary pollution to the environment or "salt dirty" phenomenon. Hence, the choice of corrosion inhibitors must not only consider the issue of environmental quality, but also pay attention to the beautification of the environment. The corrosion inhibitor in the deicing salt has freezing point after adsorbing Cl^-, which is a big breakthrough on the basis of the original. As different from other corrosion inhibitors which are difficult to biodegrade and adsorb on the road surface, the corrosion inhibitor with freezing point not only has good anti-corrosion effect, but also dissolves ice to reduce the amount of deicing salt used. Because the world pays great attention to environmental issues, it is necessary to develop high-efficiency, non-toxic and non-polluting corrosion inhibitors.

The general chemical formula of the layered double hydroxide is: $[M_{1-x}^{2+}M_x^{3+}(OH)_2]\ (A^{n-})_{x/n}\cdot mH_2O$, whose main metal elements and interlayer structures are adjustable, so LDHs' applied field is extremely extensive (Ingram and Taylor 1967; Allmann 2010). The high temperature calcined LDHs which can adsorb a large amount of anion due to "memory effect", electrostatic adsorption and high specific surface area. So, it can be used as high adsorption capacity adsorbent (Huang et al. 2017; Dan et al. 2003). Wei Ma et al. found that the Mg-Al-Fe hydrotalcite-like compound after 500 °C calcination (HTlc500) has a good removal effect on fluorine, and the adsorption data can be well fitted by the Langmuir isotherm model and the pseudo first-order kinetic model (Wang, 2011). The corrosion resistance of various forms of MgAl-LDHs synthesized on AA6082 was investigated. It is determined that LDHs have a good inhibitory effect on the corrosivity of metals (Ahsan et al. 2018). Numerous scholars have been studied the adsorption mechanism of double-layer hydroxide after high temperature burning (CLDH). It is confirmed that the CLDH's adsorption process not only has physical adsorption, but also exists chemisorption (Zheng et al. 2019). At the same time, Chao Peng et al. found that Mg-Al-LDHs can reduce solution's freezing point (Peng et al. 2015). In summary, CLDH can be used as corrosion inhibitor at low temperatures.

Hence, the main purpose of this article is to discuss the corrosion inhibition properties of $MgAlO_x$ and $MgAlFeO_x$. Then, we determined that one of them is corrosion inhibitor by comparing the corrosion inhibition performance of two substances. Finally, we used various characterization methods to

detailedly analyze the relationship between change of LDHs and corrosion inhibition performance after Fe^{3+} incorporation.

2. Material And Methods

2.1 Materials

Iron nitrate nonahydrate ($Fe(NO_3)_3·9H_2O$), aluminium nitrate nonahydrate ($Al(NO_3)_3·9H_2O$), magnesium nitrate hexahydrate ($Mg(NO_3)_2·6H_2O$), sodium carbonate (Na_2CO_3), sodium hydroxide (NaOH), calcium chloride ($CaCl_{2)}$, hydrochloric acid (HCl), and nitric acid (HNO_3), were analytical grade and were obtained from Tianjin Kermel Reagent Co. All solutions were prepared with deionized water.

2.2 Preparation of the MgAlOx/ MgAlFeOx corrosion inhibitor

Adding $Mg(NO_3)_2.6H_2O$, $Al(NO_3)_3·9H_2O$ and $Fe(NO_3)_3·9H_2O$ with different molar ratios to the beaker to form A solution with a concentration of 0.55 mol·L^{-1}. The NaOH and Na_2CO_3 were added in the beaker as the molar ratio of 3:1 to form 2.25 mol·L^{-1} as B solution. Then, the A and B solutions were simultaneously dropped into the C solution containing deionized water. At the same time, controlling the drop rate (about 1 drop/s) adjusted the pH is 9.5. The mixture was stirred vigorously for 30 min, placed in a stainless steel autoclave of Teflon, and then put in an oven at reaction temperature (80 °C, 100 °C, 120 °C) for 12 h, respectively. After the completion of the reaction, the mixture was centrifuged, washed to neutrality, dried in an oven at 80 °C for 10 h, and ground into a powder to finally obtain LDHs. The newly prepared LDHs were placed in a muffle furnace and calcined at different temperatures for 4 h, and the heating rate was 2 °C·min^{-1} to obtain composite metal oxide (CLDH). The preparation process is shown in Fig. 1.

2.3 Adsorption experiment of Cl^- by corrosion inhibitor

The corrosion resistance of metal oxides to Cl^- was determined according to batch adsorption experiments under different conditions. $CaCl_2$ was dissolved in deionized water to prepare a 100 mg·L^{-1} chloride solution. 0.2 g metal oxide was added to Erlenmeyer flask containing 100 mL $CaCl_2$ solution, then put it on the stirrer rotating at 150 rpm to carry out adsorption experiments at low temperature and room temperature, respectively. The low temperature experiment was set to 0 ± 2 °C and room's was taken at 25 ± 2 °C. Since deicing salt's residence time should not be too long, so we chose 200 min for the longest reaction time. At the same time, we considered the randomness of deicing and set different time intervals. After the experiment was completed, the solution was separated using a 0.45 μm filter, and the amount of residual Cl^- was measured by titration.

2.4 Determination of Cl^-

Firstly, pipetting 50 mL of chloride's solution into a 250 mL Erlenmeyer flask. Secondly, adding 2 drops of phenolphthalein indicator to adjust solution's pH with weak base (0.1 mol·L^{-1} NaOH) or acid (0.1 mol·L^{-1} HNO_3) solution. Then, adding 1 mL 50 g·L^{-1} K_2CrO_4 solution as indicator. Lastly, titrating with 0.1 mol·L^{-1} $AgNO_3$ standard solution under shaking conditions until brick red appeared. Simultaneously, preparing blank test for comparison. The formula for calculating the Cl^- concentration is as follows:

$$P_1 = \frac{(V_1 - V_0)cM}{1000V} \times 10^6$$

where P_1 is concentration of Cl^-, mg·L^{-1}; V_1 is the value of $AgNO_3$'s volume consumed by the titrating chlorine solution, mL; V_0 is blank test consumes the volume of $AgNO_3$ solution, mL; V is the sample's volume, mL; c is the concentration of $AgNO_3$ solution, mol·L^{-1}; M is the molar mass value of chlorine, g·mol^{-1} (M=35.45).

2.5 Corrosion inhibiting experiment

2.5.1 Dry and wet cycle test of concrete

The dry-wet cycle experiment was used to simulate the corrosion process of deicing salts under real environment. The 28-day-old concrete test block was immersed in a 5% deicing salts solution for 18 h, and then dried in an oven at 60 °C for 6 hours. A cycle of 24 h was used, and the experiment was performed for 168 h. After the dry-wet cycle is completed, the concrete peeling slag particles are collected in a beaker, rinsed with distilled water, and then dried in a 105 °C ± 2 °C oven to constant weight.

2.5.2 Carbon steel corrosion rate experiment

The corrosion of the deicing salt solution on the metal was measured by the rotating hanging method, and the corrosion rate of the deicing salt was determined by calculating the mass loss of the test piece. The carbon steel sheet used has a size of 50 mm × 25 mm × 2 mm. Carbon steel test pieces were pretreated with acetone and alcohol, then dried in an oven at 60 °C, and then suspended in 5% deicing salt solution to measure the corrosion rate of carbon steel. The solution was placed in a constant temperature water bath at a holding temperature of 30 °C, the rotation speed was adjusted, and the suspension test was stopped after 72 hours of stirring. The test piece was taken out, washed in the acid solution for 30 s, rinsed with water, immediately immersed in NaOH solution for 30 s, rinsed with water, wiped dry with filter paper, soaked in anhydrous ethanol for 3 min, wiped dry with filter paper, and placed in drying oven at 60 °C , then weighing to the nearest 0.2 mg. At the same time, the test blank pickling blank test to correct the weight loss of pickling. The corrosion rate of mixed deicing salt on carbon steel can be calculated as follows:

$$v = 8760\,(m - m_0) \times 10 / spt$$

Where v is the corrosion rate of deicing salt to carbon steel, mm/a; m is the loss weight of test piece, g; m_0 is the loss weight of pickling blank, g; s is the surface area of test piece, cm^2; p is the density of test piece, $g \cdot cm^{-3}$; t is the experimental time, h.

2.6 Test of corrosion inhibitor freezing point

$MgAlO_x$/ $MgAlFeO_x$ exists in the form of MgAl-CO_3^{2-}-LDHs/ MgAlFe-CO_3^{2-}–LDHs and MgAl-Cl^--LDHs/ MgAlFe-Cl^--LDHs in low temperature chlorine solution. Hence, when analyzing the freezing point of $MgAlO_x$ and $MgAlFeO_x$, they were placed in the solution having concentration of 100 $mg \cdot L^{-1}$. Determined the freezing point of corrosion inhibitor at 5 wt%, 10 wt%, 20 wt%, 30 wt%, and 40 wt% concentration according to the Chinese standard GB/T23851-2009 (consistent with ASTM D 1177-94) and plot the time-temperature curve. Find the projection point of the intersection of the cooling curve and the crystallization curve on the vertical axis, which is the freezing point of the sample. If there is a surfusion phenomenon, the maximum temperature reached by the temperature rise after the sample is over cooled is the freezing point of the sample. Repeated determination of the two results, the arithmetic mean as a result of the measurement, accurate to 0.1 ºC.

2.7 The determination of pH

Weighing 1.00 g ± 0.01 g sample into a 250 mL beaker, add 5 mL ethanol to wet, add 100 mL carbon dioxide-free water, stiring for mixing, then removing 100 mL solution for using. A standard buffer with a pH value close to the sample solution is used for positioning. The electrode was washed with deionized water and then with the sample solution. Adjusting the temperature of the sample solution to (25 ± 1) °C, and the temperature compensation of pH is 25 °C, too. Finally, determined the the sample solution's pH. In order to measure accurate results, the pH reading was stable for at least 1 min.

2.8 Regeneration experiment of corrosion inhibitor

The 0.2 g used corrosion inhibitor was put in 100 mL 0.28 $mol \cdot L^{-1}$ Na_2CO_3 solution, and placed the mixed solution on a stirrer for 12 h. The filter was washed with deionized water and dried in an oven at 80 °C for 10 h. Finally, the dried powder was placed in muffle furnace and calcined at 500 °C for 4 h (2 $°C \cdot min^{-1}$) to obtain the product which was again used as corrosion inhibitor. Anticorrosive resistance after corrosion inhibitor regeneration is determined by measuring its removal rate of Cl^-.

2.9 Analytical methods

The X-ray diffraction (XRD) patterns of samples were obtained using a Rigaku D/max-IIIB X-ray diffractometer with Cu Kα radiation (λ = 1.5406 °A) generated at 40 kV and 20 mA. The Brunauer–Emmett–Teller (BET) surface areas of the samples were determined using N_2 adsorption on a Micromeritics ASAP2420 instrument, and the plot of the pore-diameter distribution was determined by using the Barrett–Joyner–Halenda (BJH) method from the desorption branch of the isotherm. Analyses

of surface composition of the prepared samples were conducted using XPS (Kratos-AXIS UL TRADLD, Al KaX-ray source) and data were fitted “XPS peak” so ware. The micromorphological characteristics of samples were characterized using a Hitachi S-4800 scanning electron microscope (SEM) at an accelerating voltage of 5.0 kV. The surface charges of supported samples at pH 6.0-10.0 were determined using a zeta-potential analyser (Horiba, SZ-100Z, Japan). TG-DSC measurements were carried out using a Pyris Diamond TG/DSC instrument (Q600 SDT) with N_2 as carrier gas. The temperature was controlled within a range of 30 - 800 °C and at a rate of 2 °C·min^{-1}.

3. Results And Discussion

3.1 The effect of preparation conditions on MgAlFe-LDHs

3.1.1 Different molar ratio of [Mg]/[Al]/[Fe]

Fig. 2 (a) is the XRD diffraction pattern of samples of MgAlFe-LDHs prepared at different [Mg]/[Al]/[Fe] molar ratios. It can be seen from the figure that although the [Mg]/[Al]/[Fe] molar ratios of the respective sample is different, they all exhibit characteristic peaks of the double-layer hydroxide (Lv et al. 2019). At the same time, the difference between peak shape and symmetrical peak indicates crystallinity and phase's diversity (El-Nahhal 2003). Firstly, the samples of $[M^{2+}]/[M^{3+}]$ 2, 3 and 4 are synthesized by fixing the molar ratio of [Al]/[Fe] at 2:1. By comparing their XRD spectra, the sample with $[M^{2+}]/[M^{3+}]$ of 3 has the sharpest peak shape and the best crystallinity (Tao et al. 2018). So, it is confirmed that the value of $[M^{2+}]/[M^{3+}]$ is 3 during the sample synthesis. Samples with [Al]/[Fe] of 1,1/2,2,1/3 and 3 are synthesized on the premise of $[M^{2+}]/[M^{3+}]$ is 3. Similarly, the best ratio of [Al]/[Fe] is 2 according to the method of comparing the crystallinity of samples distributed in the same XRD spectrum (Tao et al. 2018). From the above analysis, the optimum molar ratio of [Mg]/[Al]/[Fe] is 9:2:1.

3.1.2 Different temperature of the reaction process

Fig. 2 (b) is the XRD analysis of MgAlFe-LDHs prepared at different temperatures (80 °C, 100 °C and 120 °C), respectively. Each of them exhibit characteristic diffraction peak of double layer hydroxide (Lv et al. 2019). It can be seen from 3 that when the reaction temperature is 80 °C, only the (003) and (006) crystal faces of LDHs (PDF #52-1625) are exhibited, and the corresponding peaks are not sharp and have impurities $Mg(OH)_2$ and $Al(OH)_3$.This indicates that the chemical process is not completely reactive and the crystallinity of the sample is not high (Jian et al. 2019). At 100 °C, the characteristic diffraction peaks of LDHs appear, and the (003), (006), (012), (110), and (113) crystal faces (PDF#52-1625) appear, respectively (Tao et al. 2018). But the symmetry peaks are not obvious and also exists $Mg(OH)_2$ and $Al(OH)_3$. At a temperature of 120 °C, the characteristic diffraction peaks of LDHs are exhibited, the peak shape is sharp and the symmetrical peak is obvious, and there is no other phase. It shows that the purity of the sample increases with the increase of the synthesis temperature, and the crystallinity is also ideal,

showing less content of the heterophase (Xu and Lu 2005). Therefore, 120 °C is the optimum preparation temperature.

3.1.3 The TG-DSC and calcination temperature of MgAlFe-LDHs

The thermal behavior of MgAlFe-LDHs was analyzed by TG-DSC spectroscopy in Fig. 2 (c). It can be seen from the analysis curve that there are three endothermic peaks, indicating that the thermal decomposition of MgAlFe-LDHs is mainly divided into three parts (It can be seen from the analysis curve that the thermal decomposition of MgAlFe-LDHs is mainly divided into three parts) (Ji et al. 2017). The first absorption peak rises from 30 °C to about 258 °C, mainly caused by the removal of water molecules adsorbed on the surface and between the layers . The endothermic peak between 274 °C and 445 °C is attributed to the decomposition of the inter-layered crystal water and the -OH layer and part of the CO_3^{2-}. The third absorption peak is accompanied by significant mass loss, and in the range of 466 °C to 600 °C, the interlayer anions are completely removed in the form of CO_2 and H_2O (Yang et al. 2012). Table S1 is the detailed TG-DSC results for MgAlFe-LDHs.

Fig. 2 (d) is columnar distribution of MgAlFe-LDHs' Cl^- removal rate at different calcination temperatures. It can be seen from the figure that the material removal rate after calcination at 500 °C is the highest, reaching 85.5%, which is significantly higher than the removal rate of Cl^- at other temperatures, 300 °C - 30.70%, 400 °C - 63.23%, 600 °C - 24.32%. Combined with the analysis of TG-DSC, when calcination temperature≦572 °C, MgAlFe-LDHs successively removes the the interlayer's water, the hydroxyl layer's water molecule, and CO_3^{2-}, then the metal oxide is formed after dehydration (Ji et al. 2017; Yang et ai. 2012) . This calcination produces reconstituted the layer structure by re-adsorbing anions. Therefore, the removal rate is increased along with increasing calcination temperature between 100 °C and 500 °C. When the temperature exceeds 572 °C, calcined product with the spinel structure is formed, whose structure is unrecoverable by absorbing anions, and corresponding the Cl^-'s removal rate is small (Jian et al. 2019). Hence, when the temperature reaches 600 °C, the removal rate starts to decrease. After the above analysis, it is confirmed that the optimum calcination temperature of MgAlFe-LDHs is 500 °C.

3.2 Adsorption of chloride ions by corrosion inhibitors

Since the corrosion of the chloride deicing salt is caused by Cl^- (Farnam et al. 2015b; El-Nahhal et al. 2005)), so the anticorrosion capability of corrosion inhibitor is quantitatively expressed by the removal rate of Cl^-. Fig.3 (a) is the removal rate of Cl^- by $MgAlO_x$ and $MgAlFeO_x$ at different times. It can be seen from the figure that the adsorption capacity of $MgAlO_x$ and $MgAlFeO_x$ to Cl^- is increased as time growth. When the adsorption time of $MgAlO_x$ and $MgAlFeO_x$ on Cl^- is 60 min, the removal rates are 19.71% and 39.34%, respectively. When the time is increased to 200 min, the removal rate of Cl^- by $MgAlO_x$ and $MgAlFeO_x$ increased to 58.74% and 85.50%. Analysis of the figure 6 which shows the Cl^- removal effect of

$MgAlFeO_x$ is much larger than $MgAlO_x$'s. This indicates that the doping of Fe^{3+} in $MgAlO_x$ enhances its ability to remove Cl^- (Yang et al. 2012). Therefore, MgAlFeOx is selected as a corrosion inhibitor in the chloride deicing salt.

3.3 The anticorrosion capability of corrosion inhibitor

3.3.1 Dry and wet corrosion of concrete

It can be found from the Fig. 3 (b) that when the concrete was subjected to the wet-dry cycle test in the deicing salts solution, the mass loss value of the concrete test block increased with the increase of the soaking time. Among them, the most serious mass loss was the $CaCl_2$ solution, which was 0.051 g. Compared with the other two deicing salts, the concrete test block immersed in the deicing salt solution of $MgAlFeO_x$ corrosion inhibitor had no quality damage before 120 h, and the mass loss was 0.008 g at 168 h, and there was almost no fall off. During the wet and dry cycle, due to the repeated immersion of the concrete by the deicing salt solution, the chlorine salt solution entered the concrete to cause supersaturation and crystallization, and the crystallization pressure will aggravate the concrete damage (Thaulow and Sahu 2004). Many researchers have concluded that the corrosion effect of snow melting agents is caused by chloride ions (Farnam et al. 2015a). Our analysis shows that the addition of corrosion inhibitors has greatly reduced the corrosion effect of chloride deicing salt on concrete, and the $MgAlFeO_x$ corrosion inhibitor plays a greater role in the corrosion prevention of the concrete. The reason for this result is that $MgAlO_x$ and $MgAlFeO_x$ have an adsorption effect on chloride ions in the chloride deicing salt . From 3.2, we can know that $MgAlFeO_x$ has a better adsorption effect on chloride ions; In addition, because the corrosion inhibitor adjusts the pH of the deicing salt solution on the concrete surface, it protects the $Ca(OH)_2$ in the internal structure of the concrete (Wang et al. 2006). Therefore, the $CaCl_2$-$MgAlFeO_x$ exhibits low corrosivity.

3.3.2 Carbon steel corrosion

Though the experimental method of rotating the hanging piece, the corrosion rate of carbon steel by $CaCl_2$ was 0.31 $mm{\cdot}a^{-1}$, the deicing salt solution containing the corrosion inhibitor $MgAlO_x$'s corrosion rate of carbon steel was 0.17$mm{\cdot}a^{-1}$, and the $MgAlFeO_x$ deicing salt solution's was 0.10 $mm{\cdot}a^{-1}$ (Table S2). Compared with $CaCl_2$ and $CaCl_2$-$MgAlO_x$, $CaCl_2$-$MgFeAlO_x$ reduced the corrosion of carbon steel by 67.74% and 41.18%, respectively. The analysis of the researchers found that the main reasons for the corrosion of the carbon steel by the deicing salt are as follows: First, due to the long-term immersion in the deicing salt solution, the chloride salt on the surface of the steel bar continuously accumulates. When the concentration of the chloride salt on the surface of the carbon steel exceeds a critical value, it will have a negative impact. The pH value of the solution on the surface of the steel bar is continuously reduced, and the corrosion will become more and more serious (Wang et al. 2019); Second, when a

chloride deicing salt is in contact with carbon steel, the Cl^- reacts with iron on the surface of the carbon steel and consumes the iron base on the surface of the carbon steel and cause corrosion (Zheng et al. 2018), the equation is:

$Fe^{2+} + Cl^- \rightarrow FeCl_2$ (1)

$FeCl_2 + 2OH^- \rightarrow Fe(OH)_2 + 2Cl^-$ (2)

$4Fe(OH)_2 + O_2 + 2H_2O \rightarrow 4Fe(OH)_3$ (3)

Compared with the Chloride salt, the mixed deicing salt can adsorption the Cl^- and reduce the amount of Cl^- in the solution. At the same time, the corrosion inhibitor can adjust the pH and neutralize the acidity of the solution on the surface of the steel bar. We also comprehensively analyze 3.2 to know that the corrosion rate of carbon steel by $CaCl_2$-$MgAlO_x$ is less than that of calcium chloride and $CaCl_2$-$MgAlFeO_x$.

3.4 The freezing point of $MgAlO_x$ and $MgAlFeO_x$

Fig. 3 (c) analyzes the change in the freezing point of $MgAlO_x$ and $MgAlFeO_x$ at different mass concentrations. Since LDHs ionization occurred in solution, so it would make the solution's freezing point reduce (Peng et al. 2015). It can be seen from the figure that as the concentration increases, the freezing point of $MgAlO_x$ and $MgAlFeO_x$ are decreased. When the mass concentration is 5 wt%, the freezing point of $MgAlO_x$ and $MgAlFeO_x$ are -3.3 °C and -6.2 °C, respectively. And when the concentration is increased to 25 wt%, the freezing point of $MgAlO_x$ and $MgAlFeO_x$ respectively drop to -10.0 °C are -12.0 °C. From the above analysis and the conclusion of 3.2, it can be seen that using $MgAlO_x$ and $MgAlFeO_x$ as corrosion inhibitors can not only adsorb Cl^- (Yang et al. 2012), but also reduce the corrosion and the effect of melting ice. At the same time, it can be clearly concluded that the freezing point of $MgAlFeO_x$ is lower than the $MgAlO_x$'s, and the effect of $MgAlFeO_x$ deicing is better. Therefore, we chose $MgAlFeO_x$ as an anticorrosive corrosion inhibitor.

3.5 The effect of surface charge on chloride ion adsorption

Fig. 3 (d) shows the zeta potentials $MgAlO_x$ and $MgAlFeO_x$ in an aqueous solution of various values. Since the pH condition for deicing salt is weak acid or weak base, so we choose the range of pH is 6-10. As can be seen from the figure, along with the pH increases from 6.0 to 10.0, the $MgAlO_x$'s zeta potential decreases from 25.30 to -7.94 mV, and the $MgAlFeO_x$'s also decreases from 30.30 to -1.04 mV. The isoelectric point of $MgAlO_x$ is 8.8, and $MgAlFeO_x$'s zeta potential is 9.8. Both materials have a positive charge at pH 7 (Zheng et al. 2019). From the above analysis, it is known that due to the addition of Fe^{3+}, the zeta potential of $MgAlFeO_x$ is higher than $MgAlO_x$'s, and the isoelectric point is increased, too. This

phenomenon indicate that the positive charge on the surface of $MgAlFeO_x$ is increased, and the adsorption of negatively charged anions is also enhanced (Lei et al. 2016). Hence, the removal ability of $MgAlFeO_x$ to Cl^- is stronger than that of $MgAlO_x$.

3.6 The effect of Fe^{3+} on Cl^- removal performance

3.6.1 The change of structural characteristics

Fig. 4 is the XRD diffraction spectra of uncalcined and calcined LDHs, respectively. From Fig. 4 (1), it can be seen that the typical diffraction peaks at around 11.6°, 23.3°, 34.5°, 38.7°, 46.0°, 60.2° and 61.6° correspond to characteristic features of LDHs' planes, which are (003), (006), (012), (015), (018), (110) and (113) (PDF#52-1625), respectively (Tao et al. 2018). It is indicating that both MgAl-LDHs and MgAlFe-LDHs are hydrotalcite-like compound with tipical layered structure, and the peak shape is sharp and their have symmetrical peaks (Lv et al. 2019). Fig. 4(2) shows samples after calcination at 500 °C, and characteristic peak of Fe_2O_3 appears in $MgAlFeO_x$ (PDF#01-1053). From the above analysis, it is known that Fe^{3+} mixed with MgAl-LDHs without destroying the original layered structure, owing to Fe^{3+} added to MgAl-LDHs' main metal layer plate and gets into the layer structure of MgAl-LDHs form MgAlFe-LDHs. After the incorporation of Fe^{3+}, the XRD structure parameters of LDHs are changed, and the crystallite size is increased from 182 A to 249 A (Scherrer equation). Meanwhile, as can be seen from Table S3, the interplanar spacing of each crystal face is increased (Hong et al. 2019). Since Fe^{3+} replaces Al^{3+} on a partial layer, the atomic density on the crystal plane is reduced, and the distance between metal ions in adjacent hexagonal unit cells is increased (Yang et al. 2012). So, the lattice parameter is increased . In addition, the incorporation of Fe^{3+} increases the positive charge density on the main layer, enhances the bonding force of the main layer and interlayer anionsand , increases the number of anions filled between the layers, and cause the unit cell parameter c becomes larger (Rong et al. 2016). It is known from the Bragg's Law, a = 2d (110) and c = 3d (003) that the interplanar spacing is also increased (Pourfaraj et al. 2017). So, the calcined MgAlFe-LDHs can adsorb more Cl^- due to the increase of the interlayer spacing, the interplanar spacing and the bonding force of the main layer and interlayer anionsand.

Fig. 5 is XPS survey spectra of $MgAlO_x$ and $MgAlFeO_x$. In the wide scan $MgAlO_x$ and $MgAlFeO_x$'s XPS spectra, peaks of Mg 1s, Al 2p, O 1s and C1s of $MgAlO_x$ were observed at positions 1302.05, 74.10, 531.2 and 284.6 eV, respectively. And the $MgAlFeO_x$'s Mg 1s, Al 2p, O 1s, C1s and Fe 2p are in the vicinity of 1303.20, 74.15, 530.70, 284.6 and 712.20 eV, respectively. Compared with $MgAlO_x$, $MgAlFeO_x$ containing Fe^{3+} also exhibits the analytical characteristics of double-layer hydroxide (Shan et al. 2015). At the same time, the relative content of metal elements are increased (Table S4), as shown by the fact that the peak positions of Mg 1s and Al 2p are converted to high binding energy (Fig. 5(c) and (d)) (Zou et al. 2018). There is the appearance of Fe 2p at 712.20 eV (Fig. 5(b)), and the result accords to XRD's (Zhou et al.

2011). The increase of metal elements indicates that the bonding strength of $MgAlFeO_x$ is greater and the adsorption capacity for Cl^- is better (Gao et al. 2018). Fig. 5(e) and (f) show the XPS O 1s spectral resolution of $MgAlO_x$ and $MgAlFeO_x$, respectively. The $MgAlO_x$'s O 1s can be decomposed into "Mg-O" and "Al-O" bonds. In $MgAlFeO_x$, O 1s is deconvolved into three peaks of "Mg-O", "Al-O" and "Fe-O" due to the interaction between Fe and O (Zou et al. 2018; Benchikh et al.2018). And the presence of Fe causes $MgAlFeO_x$ to adsorb more Cl^- due to increased interplanar spacing and layer spacing (Rong et al. 2016).

Fig. S1 shows the BET spectrum and pore size distribution curve of the prepared $MgAlO_x$ and $MgAlFeO_x$. According to the classification of IUPAC, the adsorption isotherms of two substances behave as typical type IV adsorption behavior and H3 hysteresis loop, with the existence of mesoporous structure (Wang et al. 2019). Table S5 shows the specific surface area, pore size and pore volume of samples. Compared with $MgAlO_x$, it can be shown that the addition of Fe^{3+} changes the textural properties of the material, the specific surface area increases from 69.2821 to 80.3931 $m^2 \cdot g^{-1}$, and the pore volume changes from 0.2891 to 0.2916 $cm^3 \cdot g^{-1}$,and this feature indicates that $MgAlFeO_x$ has a better ability to capture Cl^- (Lei et al. 2016).

3.6.2 The change of surface topography

Fig. 6 (a-d) shows SEM images of uncalcination MgAl-LDHs, MgAlFe-LDHs and after calcination $MgAlO_x$, $MgAlFeO_x$. It can be seen from (a) and (b) that uncalcined LDHs are aggregated by many lamellar structures (Jian et al. 2019). Among them, the MgAlFe-LDHs formed by the incorporation of Fe^{3+} into the original layer didn't destroy the original layered structure. However, layer's gap of the sample is increased, and the specific crystal form changes from similar octahedron layer to elliptical layer. Fig. (c) and (d) are SEM images of the two materials after calcination, and their layers are thinned and also exhibit a layered structure. Compared with $MgAlO_x$, the layer space of MgAlFeOx is significantly increased. This feature has been illustrated by XRD and BET. Fig. 6 (e) and (f) are the energy dispersive spectroscopy (EDS) and the percentage of relative elemental distribution for the two calcined materials, respectively. Analysis of Fig. 6 (e) and (f) shows that in the EDS and the Mapping analysis of $MgAlFeO_x$, the characteristic distribution of iron element appears, which indicating the existence of Fe^{3+}. At the same time, it can be seen from Table S6 that the metal elements' content of $MgAlFeO_x$ is increased, and the sample surface's positive charge density is increased, too (Yang et al. 2012; Gao et al. 2018) Therefore, the $MgAlFeO_x$ has better adsorption capacity for anions. This analysis corresponds to the results of XRD, Zeta and XPS results.

3.7 Anticorrosion mechanism of corrosion inhibitor

The anticorrosive effect of corrosion inhibitor is the effect of two aspects, as shown in Fig. 7. First, the anticorrosive effect of the corrosion inhibitor is manifested by the immobilization of free Cl^-. Soudki K A

andVerian K P et al. found that the harm of chlorine salt type deicing salt to the environment and infrastructure is caused by Cl^- (Farnam et al. 2015b; El-Nahhal et al. 2005)). $MgAlFeO_x$ can immobilize Cl^- by surface adsorption and chemisorption (Zheng et al. 2019; (Yang et al. 2012). The addition of Fe^{3+} enhanced the physical adsorption and chemical adsorption of the material, and detailed characteristics are obtained through the above zeta potential and characterization analysis. The amount of positive charge on the surface of the material increases, the BET area increases, the crystal plane spacing and interlayer spacing also increases, the metal ion content increases, and the bonding force between the main layer and the interlayer anions also increase. Hence, the final performance of material containing Fe^{3+} is increased the adsorption capacity of Cl^-. Second, the corrosion inhibitor is weakly alkaline, which can protect the internal structure of the concrete and the surface of the steel to prevent damage from chloride salts. By measuring the pH of the corrosion inhibitor, the pH of $MgAlFeO_x$ was found to be 8.2 (as shown in Table S7). Due to the $CaCl_2$'s deicing salt solution is weak acidity, it will enter into concrete interior not only reacts with pyrite ($Ca(OH)_2$) to expend the main components of concrete, but also corrodes the passive film on the surface of the steel bar and consumes the iron base of the steel bar (Kim and Hyeong-Ki 2015; Zheng et al. 2018). The corrosion inhibitor is weakly alkaline, which can release OH^- and neutralize the pH of deicing salt solution, thus achieving the anti-corrosion effect.

Conclusions

This paper discusses the use of $MgAlO_x$/$MgAlFeO_x$ as corrosion inhibitor in chloride deicing salts. The results show that when the molar ratio of Mg/Al/Fe is 9:2:1, the synthesis temperature is 120 °C, and the calcination temperature is 500 °C, the removal rate of $MgAlFeO_x$ is the highest, reaching 85.50%. At the same time, we found that compared with $CaCl_2$ and $CaCl_2$-$MgAlO_x$, $CaCl_2$-$MgAlFeO_x$ has the lowest corrosion of carbon steel and concrete, 0.008g and 0.10 $mm{\cdot}a^{-1}$, respectively. Therefore, $MgAlFeO_x$ was determined to be a corrosion inhibitor in chloride deicing salts. After a series of characterization analyses, Fe^{3+} is added to the primeval main layer of LDHs, make the surface adsorption and chemisorption of the material are enhanced , and specific features are the surface positive charge increases, the BET area increases, and the metal ion content increases, respectively. $MgAlFeO_x$ can reduce the freezing point of the solution after adsorbing Cl^- at low temperature. And its freezing point decreased from -6.2 °C to -12.0 °C as the corrosion inhibitor concentration increased.

Declarations

Declaration of Interest Statement

Ethics approval and consent to participate

Not applicable

Consent for publication

Not applicable

Availability of data and materials

All data generated or analysed during this study are included in this published article and its supplementary information files.

Competing interests

The authors declare that they have no competing interests

Funding

This work was supported by A special fund project of Harbin science and technology innovation talents research (2016RQQXJ109), Heilongjiang provincial institutions of higher learning basic research funds basic research projects (KJCX201812)Heilongjiang college student innovation and entrepreneurship training program project (201810212141), Open Project of State Key Laboratory of Urban Water Resource and Environment, Harbin Institute of Technology (No. HC201711).

Authors' contributions

All authors contributed to the study conception and design.

Conceptualization

[Dongdong Wang]; Methodology: [Dongdong Wang]; Formal analysis and investigation: [Dongdong Wang], …; Writing - original draft preparation: [Dongdong Wang]; Writing - review and editing: [Dongdong Wang], [Qi Zhu]; Funding acquisition: [Qi Zhu], [Zipeng Xing], [Lei Fang]; Resources: [Qi Zhu], [Zipeng Xing], [Lei Fang]; Supervision:[Qi Zhu], [Zipeng Xing], [Lei Fang].All authors read and approved the final manuscript.

Acknowledgements

This work was supported by A special fund project of Harbin science and technology innovation talents research (2016RQQXJ109), Heilongjiang provincial institutions of higher learning basic research funds basic research projects (KJCX201812)Heilongjiang college student innovation and entrepreneurship training program project (201810212141), Open Project of State Key Laboratory of Urban Water Resource and Environment, Harbin Institute of Technology (No. HC201711). The author gratefully acknowledges their technical and financial support.

References

Ahsan, I. M. , & Michele, F. (2018) The effect of the surface morphologies on the corrosion resistance of in situ growth mgal-ldh based conversion film on aa6082. Surface & Coatings Technology,

S0257897218308053-.

Allmann, R. (2010) The crystal structure of pyroaurite. Acta crystallographica. Section B, Structural science, 24(7), 972-977.

Amin A, Khaled F, Mohsen Q, et al. A study of the inhibition of iron corrosion in HCl solutions by some amino acids. Corrosion Science, 2010, 52(5):0-1695.

Benchikh, A. , Aitout, R. , Makhloufi, L. , Benhaddad, L. , & Saidani, B. (2009) Soluble conducting poly(aniline-co-orthotoluidine) copolymer as corrosion inhibitor for carbon steel in 3% nacl solution. Desalination, 249(2), 466-474.

Chen J, Zheng F, Zhang S (2018) Interfacial Interaction between FeOOH and Ni-Fe LDH to Modulate the Local Electronic Structure for Enhanced OER Electrocatalysis. ACS Catalysis, (8): 11342-11351.

Dan, C. , Yang, L. , Zhang, J. , Zhou, J. Z. , Yun, G. , & Hong, L. (2012) Magnetic fe3o4/zncr-layered double hydroxide composite with enhanced adsorption and photocatalytic activity. Chemical Engineering Journal, 185-186(none), 120-126.

El-Nahhal Y Z, Lagaly G (2005) Salt effects on the adsorption of a pesticide on modified bentonites. Colloid & Polymer Science283(9):968-974.

El-Nahhal, Y. (2003) Adsorption mechanism of chloroacetanilide herbicides to modified montmorillonite. Journal of Environmental Science & Health.part.b Pesticides Food Contaminants & Agricultural Wastes, 38(5), 591-604.

El-Nahhal, Y. , Lagaly, G. , & Rabinovitz, O. (2005) Organoclay formulations of acetochlor: effect of high salt concentration. Journal of Agricultural & Food Chemistry, 53(5), 1620-4.

Farnam Y (2015) Damage development, phase changes, transport properties, and freeze-thaw performance of cementitious materials exposed to chloride based salts. Dissertations & Theses - Gradworks.

Farnam Y,Sarah D,Andrew W, et al. (2015a) The influence of calcium chloride deicing salt on phase changes and damage development in cementitious materials. Cement and Concrete Composites (64) : 1-15.

Farnam, Y. , Todak, H. , Spragg, R. , & Weiss, J. (2015b) Electrical response of mortar with different degrees of saturation and deicing salt solutions during freezing and thawing. Cement & Concrete Composites (59): 49-59.

Gao Z, Sasaki K, Qiu X (2018) Structural memory effect of Mg-Al and Zn-Al layered double hydroxides in the presence of different natural humic acids: Process and mechanism. Langmuir, 34 (19).

Hao M,Hong Y,Jin T.Yong T, Bo D (2019) The physical and mechanical properties of chloride-based deicers at 0～-30 °C. Construction and Building Materials, 211:721-729.

Hong, X. , Zhu, E. , Ye, Z. , Hui, K. S. , & Hui, K. N. (2019) Enhanced phosphate removal under an electric field via multiple mechanisms on MgAl-LDHs/AC composite electrode. Journal of Electroanalytical Chemistry, (836): 16-23.

Huang, G. , Sun, Y. , Zhao, C. , Zhao, Y. , Song, Z. , & Chen, J. , et al. (2017) Water–n-buoh solvothermal synthesis of znal–ldhs with different morphologies and its calcined product in efficient dyes removal. Journal of Colloid & Interface Science, 494, 215-222.

Ingram, L. , & Taylor, H. F. W. (1967) The crystal structures of sjgrenite and pyroaurite. Mineralogical Magazine, 36(280), 465-479.

Ji H, Wu W, Li F, et al. (2017) Enhanced adsorption of bromate from aqueous solutions on ordered mesoporous Mg-Al layered double hydroxides (LDHs). Journal of Hazardous Materials, 334:212-222.

Jian Z,Bo W,Chao L, et al. (2019) Preparation of mgal layered double hydroxides intercalated with nitrite ions and corrosion protection of steel bars in simulated carbonated concrete pore solution. Corrosion Science (152) : 120-129.

Kim, Hyeong-Ki (2015) Chloride penetration monitoring in reinforced concrete structure using carbon nanotube/cement composite. Construction and Building Materials, (96): 29-36.

Lei C S, Zhu X F, Zhu B C, et al (2016) Hierarchical NiO-SiO_2 composite hollow microspheres with enhanced adsorption affinity towards Congo red in water. Journal of Colloid & Interface Science,(466) : 238-246.

Lv, X. , Qin, X. , Wang, K. , Peng, Y. , Wang, P. , & Jiang, G. (2019) Nanoscale zero valent iron supported on MgAl-LDH-decorated reduced graphene oxide: Enhanced performance in Cr(VI) removal, mechanism and regeneration. Journal of Hazardous Materials, 373: 176-186.

Nixon W (2013) Sustainable Winter Maintenance. NACE (National Association of County Engineers) Annual Meeting 4:22-24 April.

Peng C, Yu J, Zhao Z, et al. (2015) Preparation and properties of a layered double hydroxide deicing additive for asphalt mixture. Cold Regions Science & Technology, 110:70-76.

Pourfaraj R, Jamilaldin Fatemi S, Yahya Kazemi S, et al. (2017) Synthesis of hexagonal mesoporous MgAl LDH nanoplatelets adsorbent for the effective adsorption of Brilliant Yellow. Journal of Colloid and Interface Science, (508) :65-74.

Rong L,Jim W,Bao Z, et al. (2016) Enhancing phosphate adsorption by Mg/Al layered double hydroxide functionalized biochar with different Mg/Al ratios, Science of The Total Environment, (559) :121-129.

Ruza Gabriela Medeiros de Araújo Macedo a, Ndnm, A. , Jt, B. , & Rdcb, A.. (2019) Water-soluble carboxymethylchitosan used as corrosion inhibitor for carbon steel in saline medium. Carbohydrate Polymers, 205, 371-376.

Shan R, Yan L, Yang Y, et al. (2015) Highly efficient removal of three red dyes by adsorption onto Mg-Al-layered double hydroxide. Journal of Industrial & Engineering Chemistry, 21(1):561-568.

Silva, A. B. , Agostinho, S. , Barcia, O. E. , Cordeiro, G. , & D'Elia, E. (2006) The effect of cysteine on the corrosion of 304l stainless steel in sulphuric acid. Corrosion Science, 48(11), 3668-3674.

Tao, X. , Liu, D. , Cong, W. , & Huang, L. (2018) Controllable synthesis of starch-modified ZnMgAl-LDHs for adsorption property improvement. Applied Surface Science (457), 572-579.

Thaulow N , Sahu S (2004) Mechanism of concrete deterioration due to salt crystallization. Materials Characterization, 53(2-4):123-127.

Tiu, B. , & Advincula, R. C. (2015) Polymeric corrosion inhibitors for the oil and gas industry: design principles and mechanism. Reactive & Functional Polymers, (95), 25-45.

Wang, D. , Zhu, Q. , Su, Y. , Li, J. , Wang, A. , & Xing, Z. (2019) Preparation of MgAlFe-LDHs as a deicer corrosion inhibitor to reduce corrosion of chloride ions in deicing salts. Ecotoxicology and Environmental Safety, (174) : 164-174.

Wang K, Nelsen D E, Nixon W A (2006) Damaging effects of deicing chemicals on concrete materials. Cement & Concrete Composites, 28(2):173-188.

Wang, T. R. (2011) Removal of fluoride ions from aqueous solution by the calcination product of Mg-Al-Fe hydrotalcite-like compound. Desalination, 268(1):20-26.

Warner L, Ayotte D.(2015) The quality of our Nation's waters: water quality in the glacial aquifer system, northern United States, 1993-2009. Circular .

Xu P, Lu Q (2005) Hydrothermal Synthesis of Layered Double Hydroxides (LDHs) from Mixed MgO and Al_2O_3: LDH Formation Mechanism. Chemistry of Materials, 17(5):1055-1062.

Yang, Y. , Gao, N. , Chu, W. , Zhang, Y. , & Yan, M. . (2012) Adsorption of perchlorate from aqueous solution by the calcination product of Mg/(Al–Fe) hydrotalcite-like compounds. Journal of Hazardous Materials, 209-210(Mar.30), 318-325.

Zheng G, Qi Z, Chun L (2018) Preparation of Ca-Al-Fe deicing salt and modified with sodium methyl silicate for reducing the influence of concrete structure. Construction and Building Materials, (172): 263-271.

Zheng, Y. , Cheng, B. , You, W. , Yu, J. , & Ho, W. . (2019) 3D hierarchical graphene oxide-nife ldh composite with enhanced adsorption affinity to congo red, methyl orange and cr(□) ions. Journal of Hazardous Materials, 369(5), 214-225.

Zhou, J. , Zhi, P. X. , Qiao, S. , Qiang, L. , & Qian, G. (2011) Enhanced removal of triphosphate by MgCaFe-Cl-LDH: Synergism of precipitation with intercalation and surface uptake. Journal of hazardous materials, 189(1-2), 586-594.

Zou, Y. , Wang, X. , Wu, F. , Yu, S. , Hu, Y. , & Song, W. , et al. (2016). Controllable Synthesis of Ca-Mg-Al Layered Double Hydroxides and Calcined Layered Double Oxides for the Efficient Removal of U(VI) from Wastewater Solutions. ACS Sustainable Chemistry & Engineering, acssuschemeng, 6b02550.

Figures

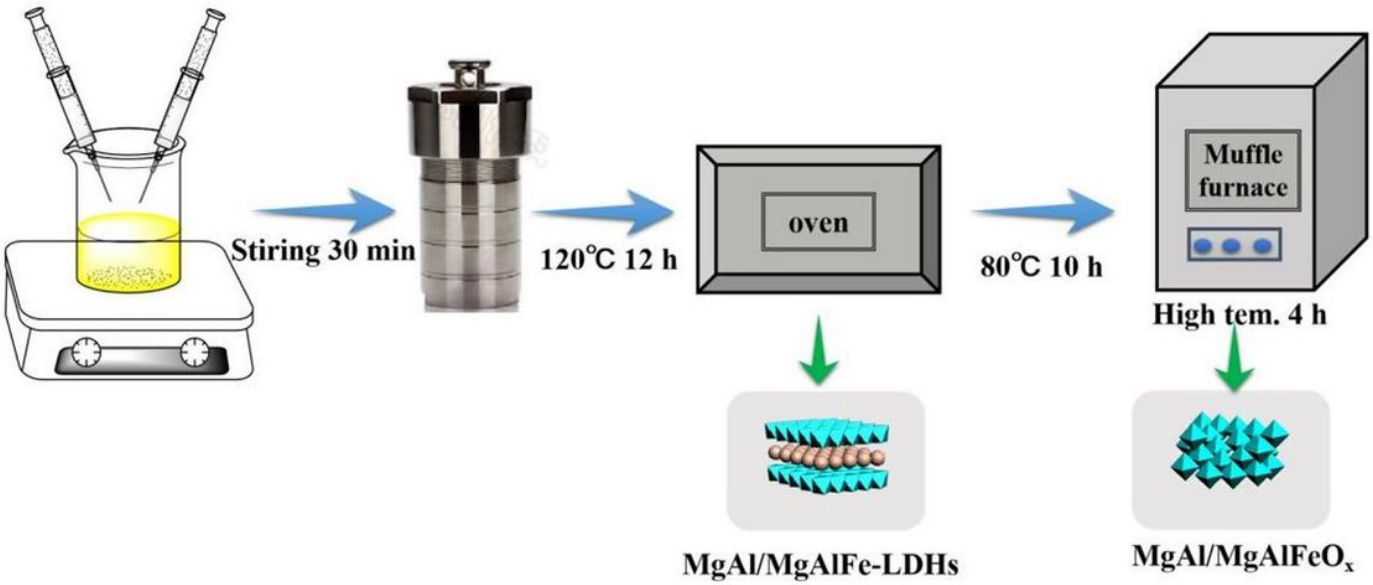

Figure 1

Preparation flow chart of corrosion inhibitor

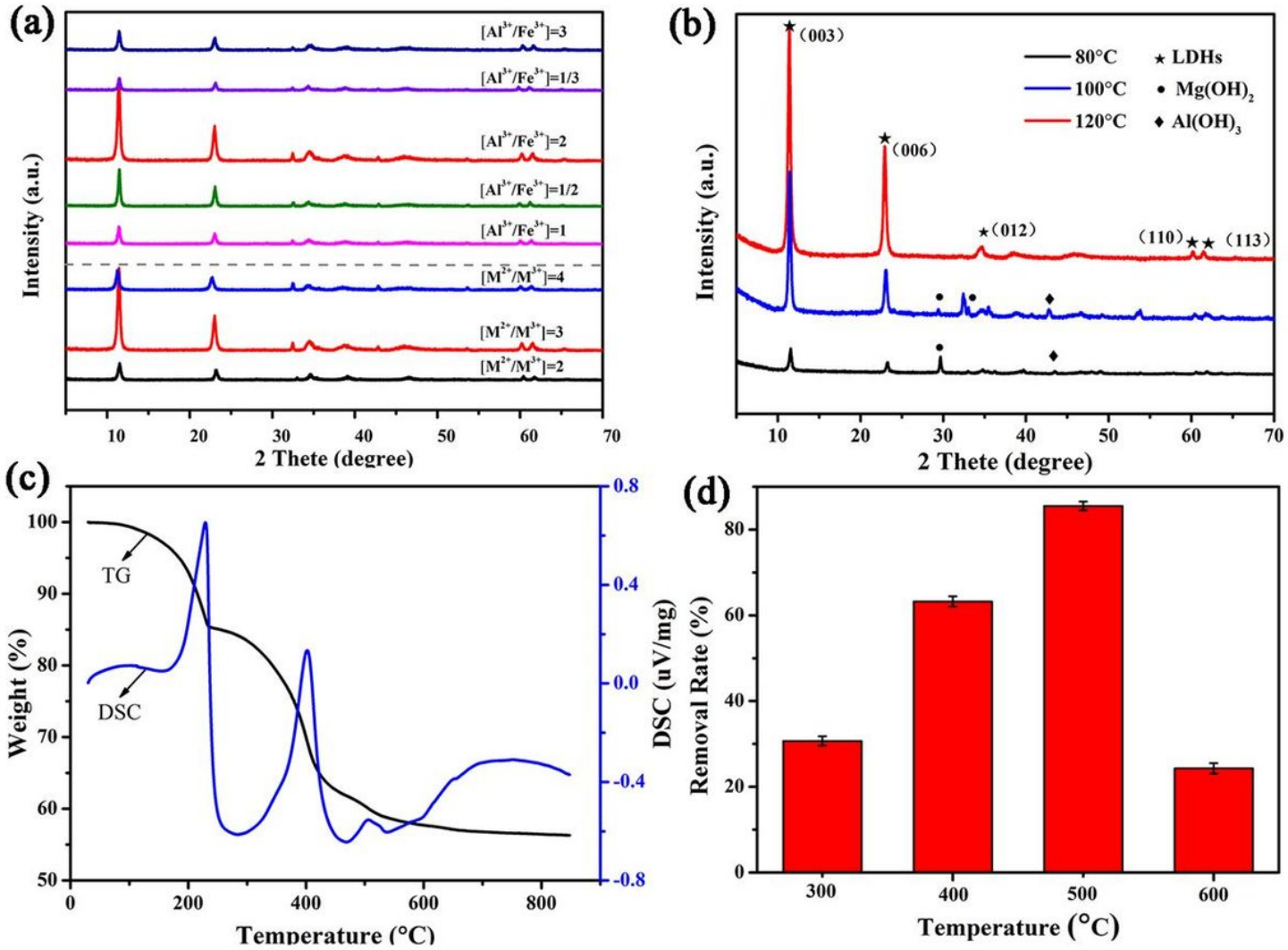

Figure 2

MgAlFe-LDHs' XRD patterns of prepared by different [Mg]/[Al]/[Fe] molar ratio (a) and different reaction temperatures (b); TG-DSC analysis (c); removal rate of Cl- at different calcination temperatures (d)

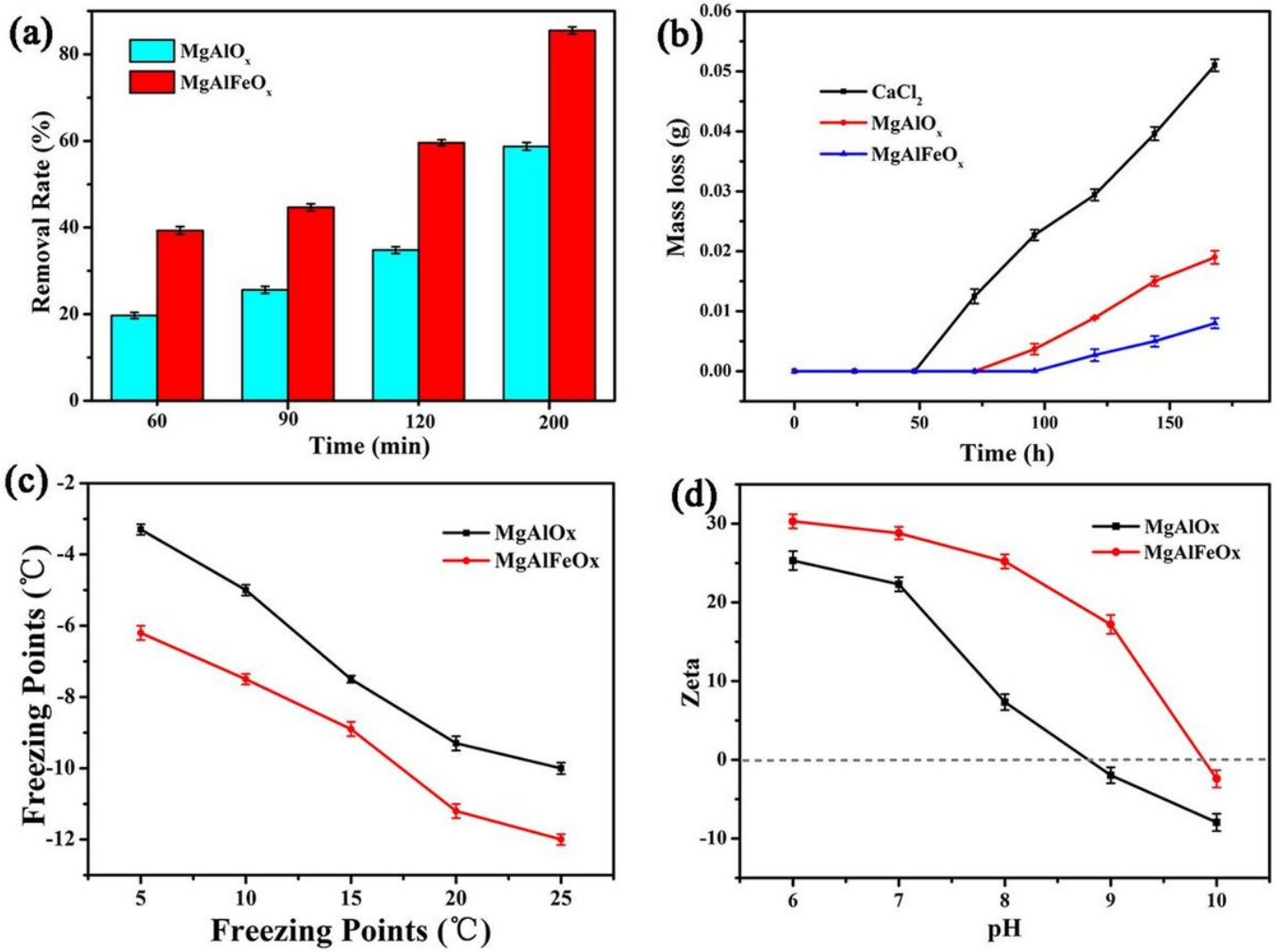

Figure 3

The Cl- removal rate (a), freezing point (b) and zeta potentials (d) by MgAlOx and MgAlFeOx; mass loss of concrete in deicing salts solution (c)

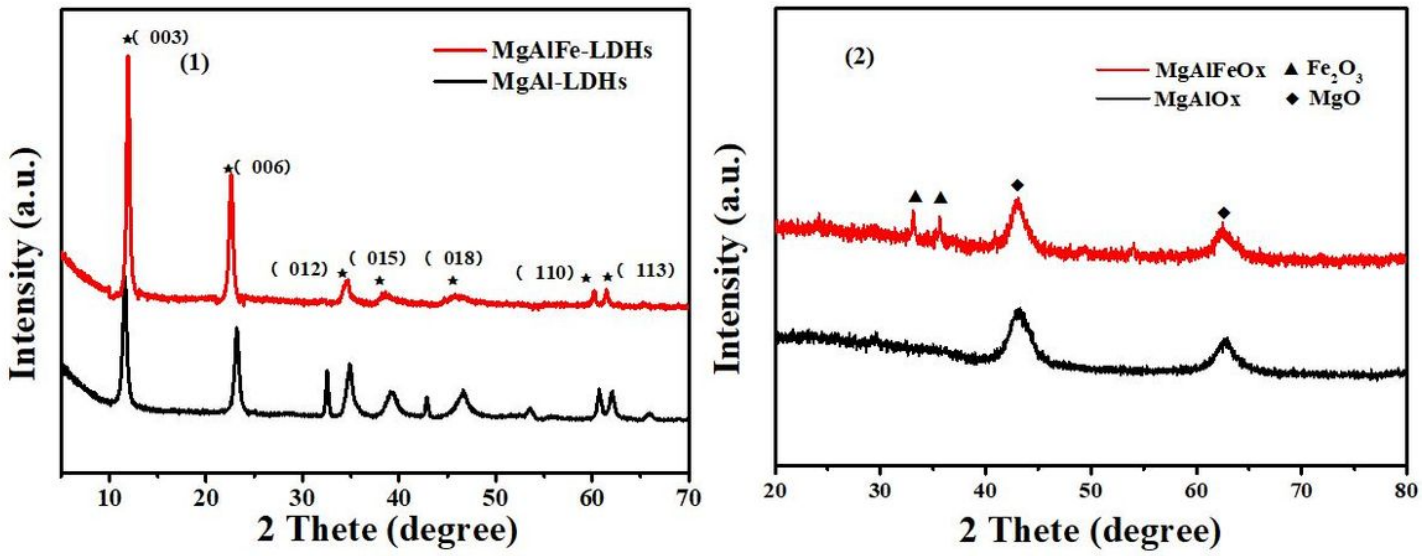

Figure 4

XRD patterns of MgAl-LDHs and MgAlFe-LDHs (1), MgAlOx and MgAlFeOx (2)

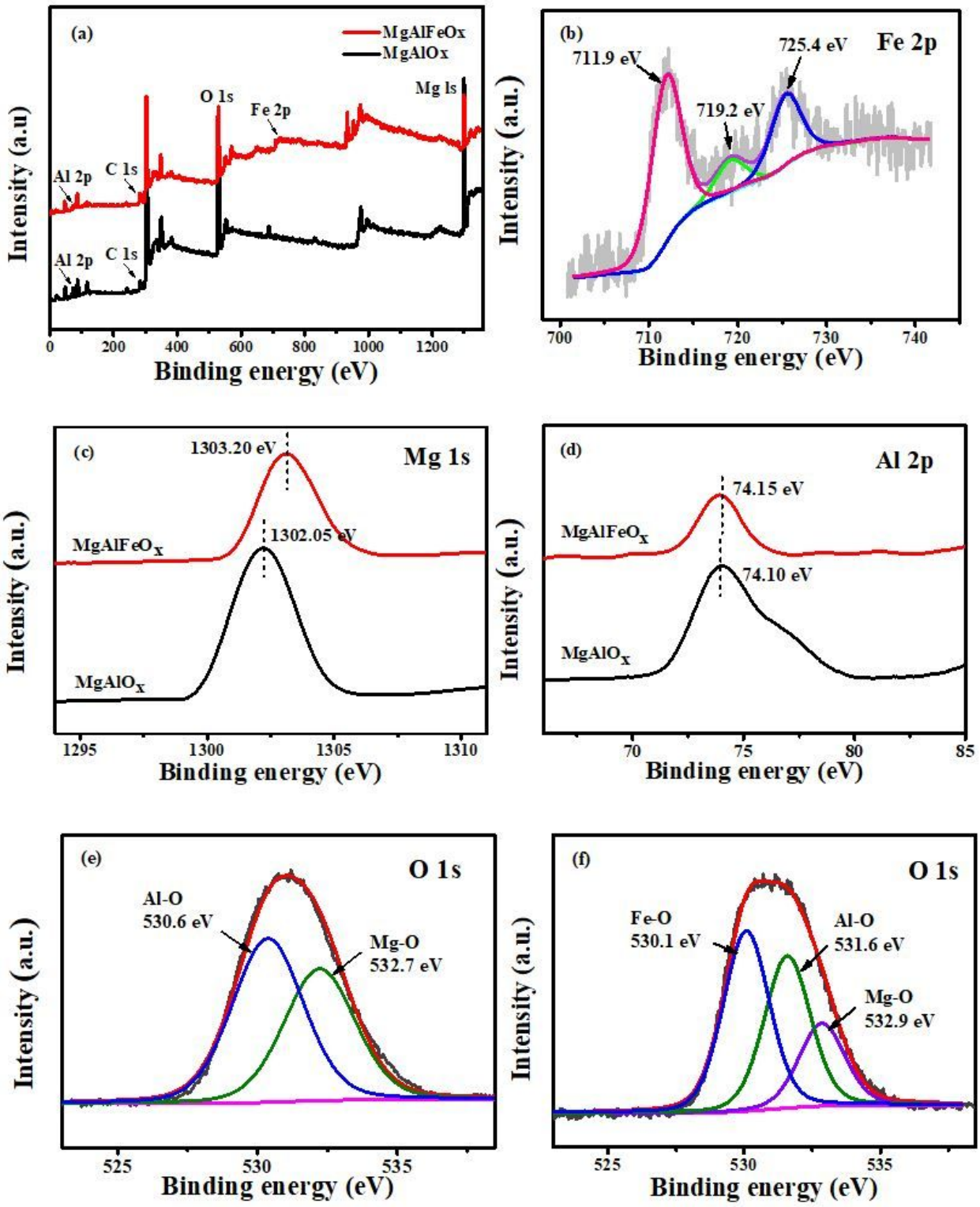

Figure 5

(a) The XPS survey spectra, (c) Mg 1s and (d) Al 2p MgAlOx and MgAlFeOx, (b) Fe 2p spectra of MgAlFeOx, O 1s spectra of (e) MgAlOx and (f) MgAlFeOx

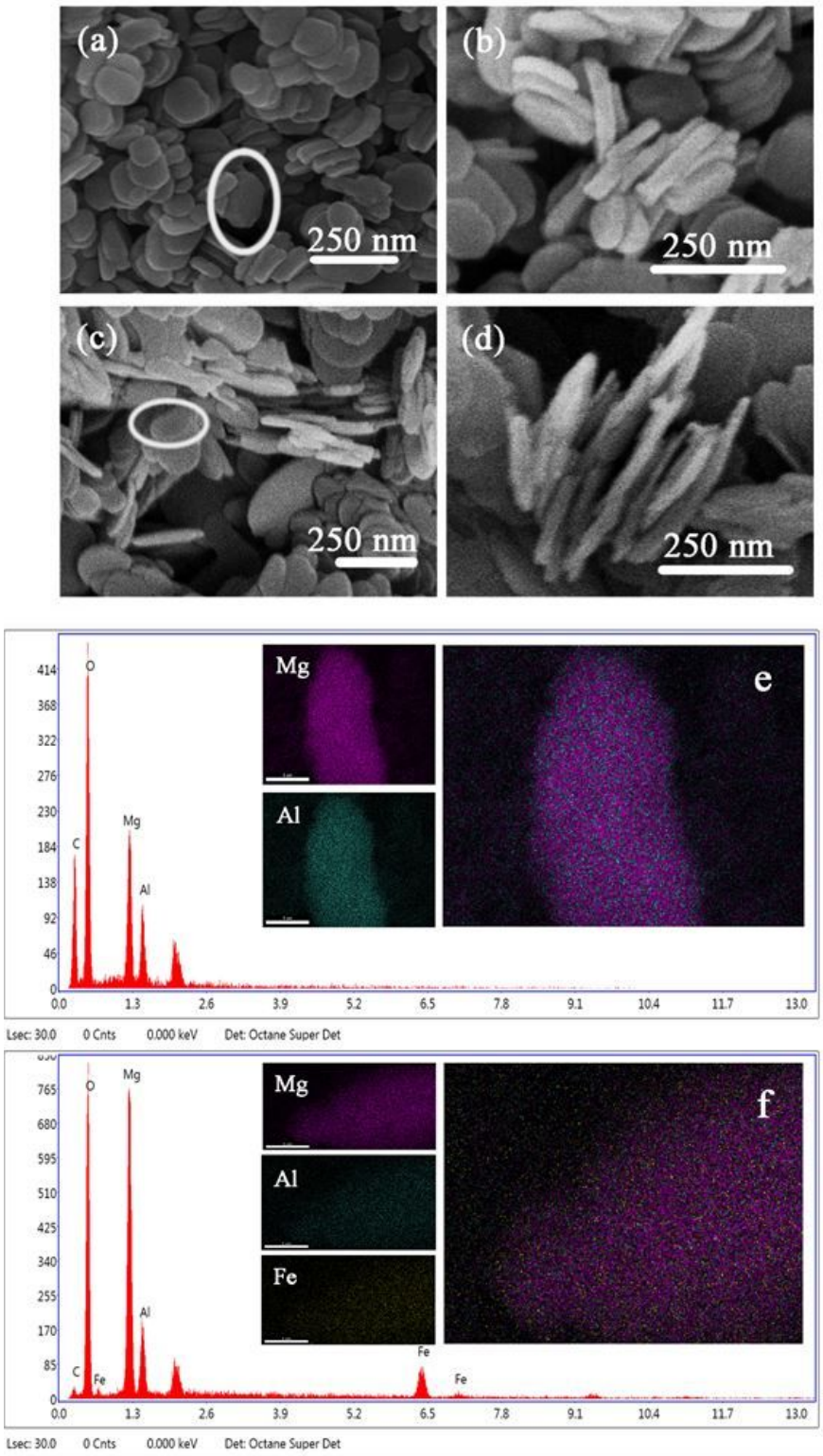

Figure 6

SEM images of MgAl-LDHs (a), MgAlOx (b), MgAlFe-LDHs (c) and MgAlFeOx (d); And EDS images of MgAlOx (e) and MgAlFeOx (f)

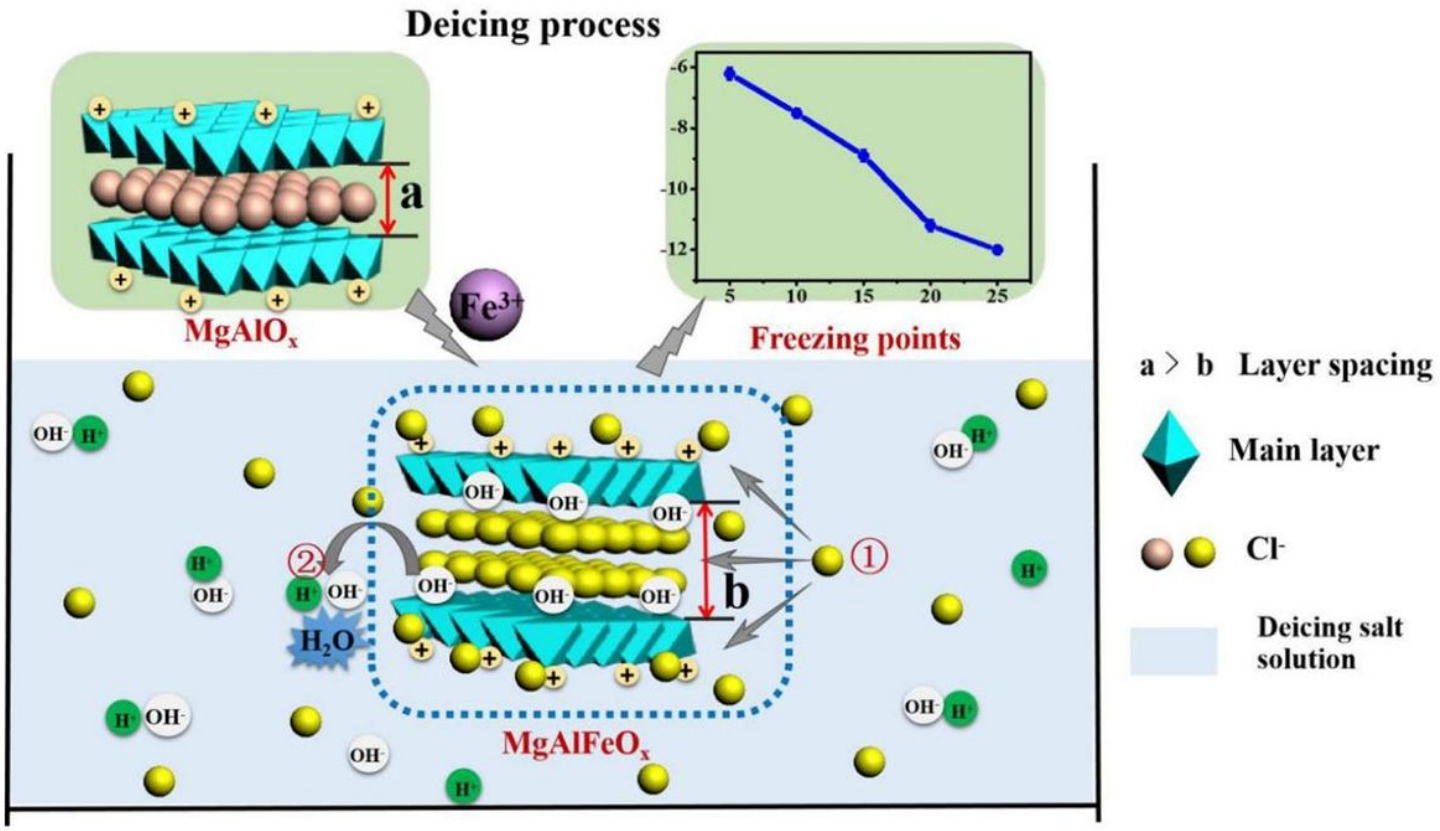

Figure 7

The anticorrosion mechanism of corrosion inhibitor

Supplementary Files

This is a list of supplementary files associated with this preprint. Click to download.

- Supplementarymaterial.doc